



Zebra rocks: compaction waves create ore deposits

Ulrich Kelka, Manolis Veveakis, Daniel Koehn, Nicolas Beaudoin

► To cite this version:

Ulrich Kelka, Manolis Veveakis, Daniel Koehn, Nicolas Beaudoin. Zebra rocks: compaction waves create ore deposits. Scientific Reports, 2017, 7 (1), <10.1038/s41598-017-14541-3>. <hal-02193034>

HAL Id: hal-02193034

<https://hal.science/hal-02193034v1>

Submitted on 24 Jul 2019

HAL is a multi-disciplinary open access archive for the deposit and dissemination of scientific research documents, whether they are published or not. The documents may come from teaching and research institutions in France or abroad, or from public or private research centers.

L'archive ouverte pluridisciplinaire **HAL**, est destinée au dépôt et à la diffusion de documents scientifiques de niveau recherche, publiés ou non, émanant des établissements d'enseignement et de recherche français ou étrangers, des laboratoires publics ou privés.



HAL Authorization

SCIENTIFIC REPORTS

OPEN

Zebra rocks: compaction waves create ore deposits

Ulrich Kelka¹, Manolis Veveakis², Daniel Koehn¹ & Nicolas Beaudoin¹

Nature has a range of distinct mechanisms that cause initially heterogeneous systems to break their symmetry and form patterns. One of these patterns is zebra dolomite that is frequently hosting economically important base metal mineralization. A consistent generic model for the genesis of these periodically banded rocks is still lacking. In this contribution, we present for the first time a fully consistent mathematical model for the genesis of the pattern by coupling the reactive fluid-solid system with hydromechanics. We show that visual banding develops at a given stress and host-rock permeability indicating that the wavelength and occurrence of the pattern may be predictable for natural settings. This finding offers the exciting possibility of estimating conditions of formation of known deposits as well as forecasting potential exploration targets.

Banded, striped or wave-like patterns are very common in natural systems and can develop spontaneously in chemical reactions. They are found on animal skins and shells¹ as well as in a variety of fluids and solids. The genesis of such patterns is linked to the formation of waves, in a system far from equilibrium. For example, a reaction-diffusion process develops waves, where a fast reaction precipitates a band of a mineral phase while diffusion depletes the surroundings in the respective reactants. The repetition of this process leads to the formation of several bands with a distinct spacing, an example of so-called self-organization. One of the fundamental works that was published on stationary waves or bands, goes back to Alan Turing² in 1952. He introduced a reaction-diffusion system in which a pattern (Turing pattern) develops as a result of instabilities in the underlying reaction.

The formation of stationary wave-like patterns is very common in geosystems³. Examples are compositional layering in igneous or metamorphic rocks, layering during sedimentation, chemical banding including the banded iron formation⁴, Liesegang rings on fracture surfaces⁵ and in ore deposits⁶, as well as layering in fault and shear zones⁷. The studies of such nonlinear dynamic systems in geosciences gave rise to the concept of geochemical self-organisation^{8,9} in which patterns develop spontaneously out of initially unordered systems. Recent advances include stress-induced effects producing not only compositional bands but also a layering in porosity^{10,11}.

A striking example of waves in rocks is the zebra texture, a pattern that can be found in a variety of rock types ranging from claystones¹², siderite^{13,14} and sphalerite mineralization¹⁵ to hydrothermal dolomite formations^{15–23}. In this work, we focus on the latter case, in which the texture of the periodic banded dolomites (zebra dolomites) consists of alternating dark and light bands (Fig. 1). The zebra texture in dolostones is frequently associated with base metal deposits of the Mississippi Valley-Type (MVT)²⁴, whereby the banding predates the ore precipitation^{25,26}.

What the underlying processes of the pattern formation in zebra dolomites are, is still debatable. Hypothesis on their genesis vary from the development of a fracture network¹⁸; opening of bedding/cleavage planes²⁷; the development of a near-horizontal set of microfractures, along which dolomite precipitates²⁵; pre-existing sedimentary partings²¹; sedimentary structures such as corals²⁵; displacive vein growth^{19,28} or a form of geochemical self-organization¹⁶. In most of the areas where zebra dolomites are found, implications for an over-pressurized hydrothermal system^{25–27} can be observed, and zebra layers frequently form parallel or at a low angle to the bedding/foliation^{18,22,27}.

The purpose of this communication is to present a physically and chemically coherent model of zebra formation in a stressed sedimentary basin with evolving fluid pressure. Our model shows that the formation of rhythmic banded dolomites is the result of compaction instabilities that arise during a reaction-diffusion process in a system under applied stress, and that these instabilities can be mathematically described by periodic waves

¹School of Geographical and Earth Sciences, University of Glasgow, Glasgow, United Kingdom. ²School of Petroleum Engineering, University of New South Wales, CSIRO Energy and Minerals Sector, Sydney, Australia. Correspondence and requests for materials should be addressed to U.K. (email: u.kelka.1@research.gla.ac.uk)

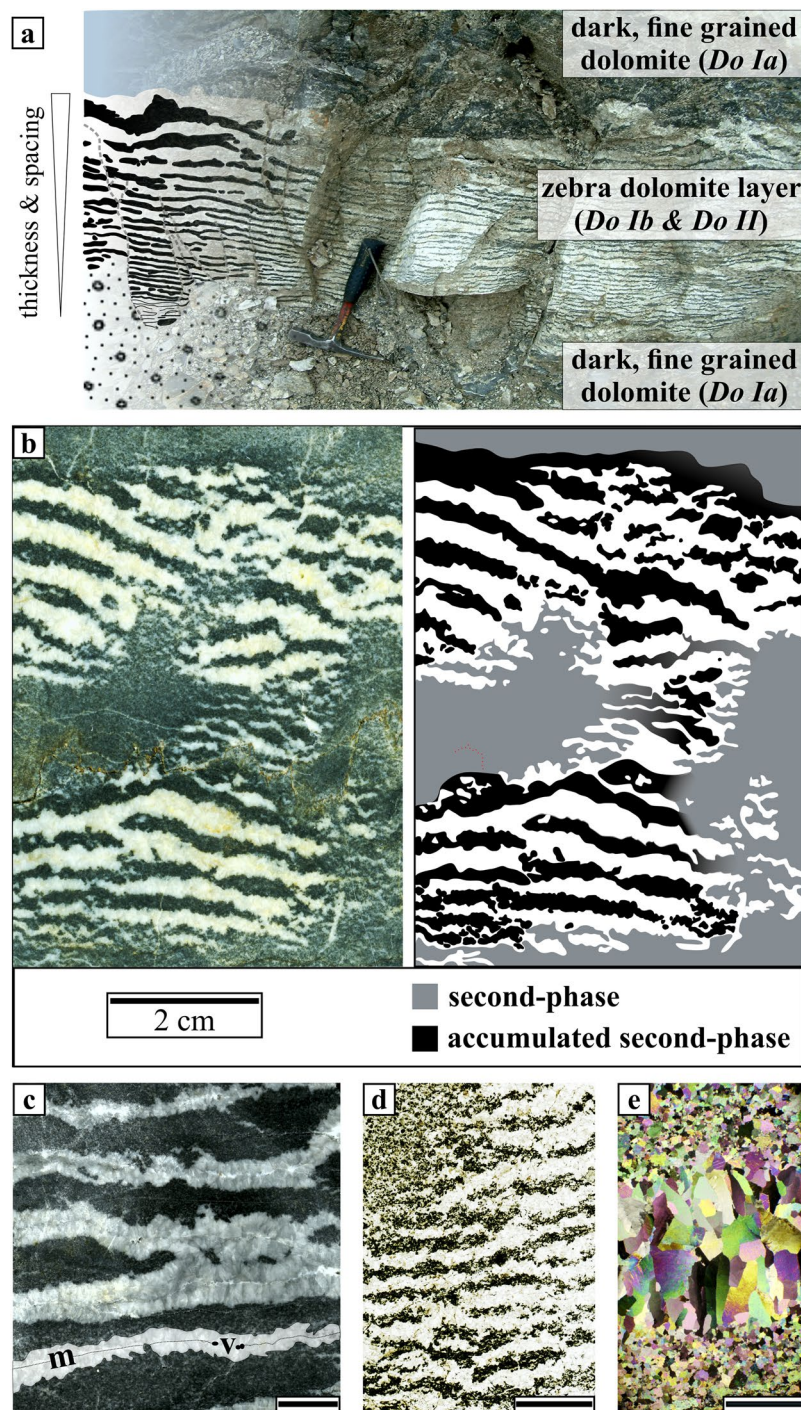


Figure 1. (a) Interpretative sketch and photograph of an outcrop of zebra dolomite layers at the San Vicente mine. Note that below and above the structure massive dark dolomite is visible. The width of the zebra dolomite layer is about 50 cm. (b) Scan of a polished hand specimen collected at the San Vicente mine and simplified sketch of the structure. (c) Scan of a polished hand specimen showing the detailed appearance of the zebra dolomite layers. The dark dolomite (*Do Ib*) alternates with light layers (*Do II*). In the central part of *Do II* a median line (*m*) with vugs (*v*) is observable (scale bar: 1 cm). (d) Scan of a thin section with thin narrow spaced zebra dolomite bands. In the upper left dark fine-grained dolomite is visible which does not show an impurity density as high as in the layers inside the zebra texture (scale bar: 1 cm). (e) Micrograph (XPL) of a single zebra dolomite layers with fine grained dolomite (*Do Ib*) below and above the coarse grained band (*Do II*) in the center (scale bar: 500 μm).

(cnoidal waves, see Fig. 2). Our 1D-model merges all existing hypothesis, and explains the typical structural features of the zebra texture in dolomites. Moreover, it is able to predict under what conditions they form.

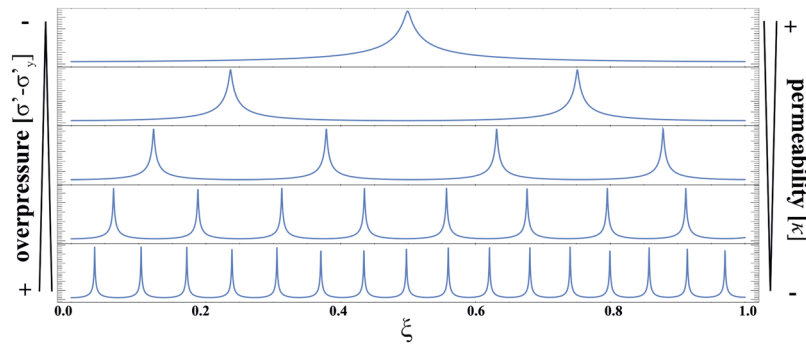


Figure 2. Response of the numerical solution of equation 3 to different overpressure ($\sigma' - \sigma'_y$) and permeability (κ) at the scaled position (ξ). With increasing depth, the overpressure rise and the permeability will decrease. However, upwelling fluids that are confined within the host-dolomite by an overlying impermeable layer (e.g. shale cap) could as well generate the overpressure. Such structures are considered to indicate good potential for MVT-deposits⁵⁶.

Zebbras in mineralized dolostones. The MVT is a mineralization type that is typically hosted in carbonate formations of sedimentary basins that often contain dolomite²⁹. While the lithology is relatively consistent, the orogenic type in which these deposits form varies (collisional, Andean or transpressional)³⁰. The tectonic regime is therefore unlikely to be a first order control of MVT mineralization, or the zebra pattern formation. However, there is a spatial and temporal relation to orogenic foreland basin development reported for the mineralization³¹.

Field observations and the analysis of hand specimens show that a high variation in spacing and thickness of the bands exists on the outcrop scale. The distance between the centres of two light layers can vary between 2 mm to 10 cm (Fig. 1a). Laterally, the bands can extend as far as tens of meters and they can merge forming dislocation or cross-bedding like patterns. The bands also exist as isolated patches of layers confined by uniform dark dolomite (Fig. 1a). The dark matrix dolomite (*Do Ia*) is thought of originating from the replacement of the initial limestone^{16,17,19,20,28} and can be regarded as the host rock of the zebra dolomite. This dark dolomite is still lighter than dark dolomite bands (*Do Ib*) that are located in between the light bands (Fig. 1b,d). On the hand-specimen scale the light layers (*Do II*) display a median line (*m*) along which a vuggy porosity (*v*) is visible (Fig. 1c). In some areas, the centres of the light bands are filled with a late carbonate phase, which can be distinguished by the lighter colour of the material (Fig. 1c). The variability of the band spacing and thickness is assessable by comparing Fig. 1c,d: the spacing in Fig. 1c is about 1 cm in width whereas it is only about 2–3 mm in Fig. 1d. On the micro scale, a closer look at a single layer under cross-polarized light (Fig. 1e) reveals that the crystal's size differs by several orders of magnitude between the fine-grained (*Do Ib*) and the coarse-grained layer (*Do II*). The fine-grained dolomite (in the dark bands) contains a large amount of impurities, which are partly clustered at the grain boundaries whereas the light layers are almost impurity free. In addition to that, the dolomite crystals in the coarse-grained light layers are elongated towards the central line, along which the void-filling carbonate cement is frequently observed^{16,25,26,32}.

The samples analysed in this study were collected at the San Vicente mine (Peru) that represents one of the world's largest ore deposits of the MVT³¹. The mine is located in the Subandean fold-and-thrust belt of the eastern Andean cordillera located about 300 km east of Lima. The hydrothermal mineralization consists primarily of the sulphide ore minerals galena and sphalerite. The ore bodies are strata-bound and hosted in Triassic/Jurassic platform carbonates (*Pucara Group*) in the western flank of the NW-SE striking *Pucara basin*. Faults likely provided pathways for the dolomitizing as well as mineralizing fluids^{33,34}. The strata that host the mineralization are over-thrusted by younger plutonic rocks (*Tamra Granodiorite*). The setting of the San Vicente mine shows several of the typical features of environments hosting MVT mineralization³¹ and can therefore be regarded as a representative study area for the formation of banded dolomites and their relationship to mineralization.

Theoretical description of pattern formation. In this section, we describe the development of the bands in the zebra dolomites by a phase separation process based on the *Cahn-Hilliard* and *Allen-Cahn* reaction-diffusion equations coupled with hydromechanics to mimic the pattern formation in a stressed sedimentary basin that undergoes diagenesis and builds up high fluid pressures. A reaction that can explain the virtually impurity-free dolomite in the light layers and the accumulation of impurities between these layers is the replacement of the primary dolomite by a secondary dolomite. While the dark dolomite (*Do Ia* & *Do Ib*) formed by the replacement of limestone will still contain impurities initially present in the rock, the replacement of the primary by the secondary dolomite (*Do II*) will segregate the impurities from the solid into the fluid (phase separation). Such a replacement reaction can be described as a process of coupled dissolution precipitation³⁵ during which the impurity rich dolomite is locally dissolved and replaced by impurity free dolomite, thus leaving the impurities in the fluid. In the actual rock, this process takes place during grain growth in which impurities are collected in grain boundaries across which the dissolution-precipitation takes place and newly grown parts of grains become impurity free. In the natural samples, this process is indicated by the accumulation of impurities on grain boundaries in the dark layers. In addition to that, grains located at the transition between dark and light

regions exhibit a sharp transition from an impurity rich nucleus within the dark bands to virtually impurity free crystals that grow towards the centre of the light layer (see Figure S4 in the supplementary material). The accumulation of impurities in the fluid can be regarded similar to industrial zone refining during which impurity-free crystalline materials are produced by a moving melting-freezing front³⁶. That impurity rich layers in rocks can be the result of a similar mechanism had already been suggested by Krug *et al.*¹³. Effective cleansing and impurity redistribution by dissolution-precipitation can be achieved in rocks during grain growth as pointed out by Jessell *et al.*³⁷. The basis of our model is a generic phase separation process that can be described as:



In the case of the zebra dolomites AB_s represents the initial dark impurity rich dolomite (dolomite I) that is of replacive origin. The phase separation is driven by a fluid that accumulates impurities during dolomite-dolomite replacement (B_f) and leaves behind an impurity-depleted dolomite phase (A_s) after the reaction. The dark layers of the zebra texture are formed during the replacement of calcite by dolomite^{19,20,25,26,28,32}, with an example shown in the supplementary material (Figure S4 in the supplementary material). The replacive origin of the primary impurity-rich dolomite (AB_s) is shown by the preservation of initial sedimentary features (Ooids) in the dark bands¹⁹. The second dolomite generation of the light zebra bands (A_s) appears as a coarse-crystalline impurity-free phase indicating an inverse correlation between final grain size and impurity density.

Typical MVT-fluids¹⁹ that are acidic, out of equilibrium with respect to the carbonate host-rock will enhance the recrystallization rates. This could explain why zebra dolomites are predominantly encountered within MVT districts. An Arrhenius law defines the mass production rate during grain coarsening. The rate of the reaction (r) can be written in a generic form as:

$$r = K_0 e^{-\left[\frac{E+P}{RT} V\right]} \quad (2)$$

In this expression, K_0 is a material specific rate constant, E is the activation energy of the process, P is the pressure related to the volume change process, V the activation volume of the reaction (which can be grain size dependent), R is the ideal gas constant and T is the temperature. Grain coarsening, as well as the dissolution of minerals in rocks, is a stress and grain size dependent process³⁸. At elevated pressures, the dissolution rate will be higher than the precipitation rate and therefore we can consider the precipitation as the rate controlling mechanism of a coupled dissolution-precipitation reaction. The formulation of the model is based on a mixed mass balance expression for the solid-fluid system, derived from initially defined partial densities for the solid (ρ_s) and the liquid (ρ_f) phase respectively. All the derivations are detailed in the supplementary material. The model represents an extension of the classical compaction bands theory³⁹ to a viscous non-linear rheology, similar to Veveakis *et al.*^{40,41} and Weinberg *et al.*⁴². We apply the equation of state on the expression of the mixed mass balance and assume isothermal conditions ($dT=0$). We can further lower the complexity by reducing the problem to 1D and considering the steady-state limit ($d/dt=0$). We then derive:

$$\frac{\partial^2 P}{\partial \xi^2} + Pe \left(\frac{\partial P}{\partial \xi} \right)^2 - \lambda P^m + \mu e^{\alpha P} = 0 \quad (3)$$

$$Pe = \beta_2 \sigma_0 \quad (4)$$

$$\lambda = \frac{\mu_f \dot{\epsilon}_0 \gamma_0^2}{k \sigma_0} \quad (5)$$

$$\mu = \lambda \frac{K_0}{\dot{\epsilon}_0} \left(\frac{\rho_s}{\rho_f} - 1 \right) (1 - \varphi) e^{-\left(\frac{E - \sigma_0 \Delta V}{RT} \right)} \quad (6)$$

$$\alpha = \frac{\sigma_0 \Delta V}{RT} \quad (7)$$

In the expression P denotes the normalised over-pressure $\left(P = \frac{\sigma' - \sigma'_Y}{\sigma_0} \right)$, ξ is the normalized space ($\xi = \frac{y}{\gamma_0}$, with γ_0 being the reference length scale) in a coordinate system moving with respect to the direction of compaction, Pe is the Peclet number and m is the stress exponent. The remaining identities λ , μ and α in equations 4–6 include the hydromechanical parameters (Table S1 in the supplementary material) whose values are stated in the caption of Fig. 3 and Table S2 (supplementary). Additional information on the development of equation 3 can be found in the supplementary materials.

The solution of expression 3 can include non-linear periodic waves given by an elliptic function. The power law exponent m in equation 3 dictates whether the solution is the *Jacobian*- (odd numbers) or the *Weierstrass*-function (even numbers)¹¹. How both are related as elliptic functions was pointed out by Abramowitz *et al.*⁴². The wave peaks appear as equidistantly spaced stress singularities (elevated fluid pressure) where dissolution takes place, thus correlating with high permeability channels⁴⁰ (for more details see Alevizos *et al.*⁴³): The genesis of these hydromechanical instabilities represents the response of the solid-fluid system to compaction,

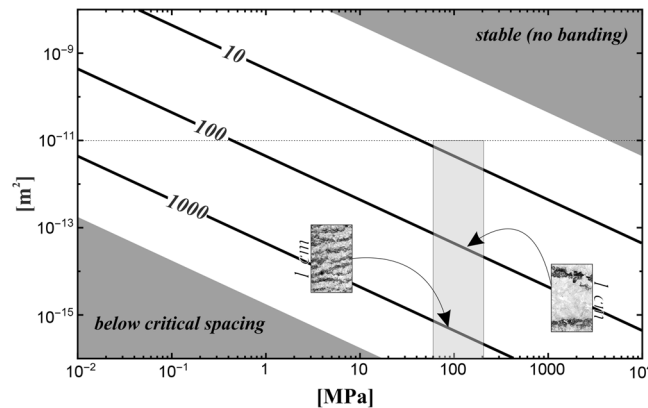


Figure 3. Log-log plot of permeability and over-pressure derived from equation 3 for a high saline brine at $T = 80^\circ\text{C}$, $\mu_f = 480\ \mu\text{Pas}$ ⁵⁷, $\rho_s = 2.9\ \text{g/cm}^3$, $\rho_f = 1.26\ \text{g/cm}^3$, $A = 5 \cdot 10^{-7}\ \text{mol m}^{-2}\ \text{s}^{-1}$ (interpolation of experiments⁵⁸), and the activation energy for dolomite precipitation $E = 31.9\ \text{kcal/mol}$ ⁵⁹. The lines indicate the numbers of zebra layers per m that can be related to the spacing of respective bands (images). The grey shaded area indicates the appropriate condition for buried dolomites. The dotted line indicates the maximum value for dolomite permeability⁴⁶.

whereas the formation of the instabilities does not need to appear simultaneous but is closely related to the solution of the wave equation. As discussed in the supplementary material, the solution is very weakly depending on the value of Pe , for the selected range of values of the parameters listed in Table S2 (supplementary). It therefore can be concluded, that the solution depends mainly on the parameters that include permeability and mean stress.

The dependence of the solution to equation 3 on stress (depth) and permeability is shown in Figs 2 and 3. The number of wave peaks grows with increasing depth and/or decreasing permeability. This consequently means that the amount of compaction instabilities (the number of light bands) or the amount of waves that occur in a fluid saturated rock, as described by equation 3, is a function of permeability and vertical stress.

Scaling to field observations. The value of λ in equation 3 is critical as it includes the hydromechanical parameters, fluid viscosity and permeability, as well as the reference values for strain, stress and space. We further notice that λ has the highest impact on the solution of equation 3. In order to invert for the spacing between the light layers we fitted λ to the number of wave peaks (NB) for constant values of μ and α . By inserting appropriate values, it can be shown that the values of the latter two dimensionless parameters are relatively low and have only little influence on the result. We obtained a square root dependency for $NB = C\sqrt{\lambda}$ where C is a constant weakly depending on the value of α (see Figure S3 in the supplementary material). For typical values, we can accept $C = 0.27$. This scaling for the number of bands can lead to a second scaling for their spacing (h), related to the compaction length⁴⁰ $h = \delta_c/C = \frac{1}{C} \sqrt{k \frac{\sigma_0}{\mu_f \dot{\epsilon}_0}}$ found in the classical compaction bands theory³⁹. With this value, it is possible to obtain a relationship to the spacing (h) and directly compare the prediction of our model to field data. The detailed description of the inversion routine can be accessed in the supplementary material section.

We applied fixed values of reference strain rate ($\dot{\epsilon}_0$), reference stress (σ_0) and of the material parameter such as density, viscosity, dissolution rate, and activation energy (see Table S2 in the supplementary material). It is important to note that the experimental determination of the energy parameter can reach uncertainties of 200–300%⁴⁴. As this value is included in the dimensionless parameter α we performed a sensitivity analysis to assess possible influences (Figure S3 in the supplementary material). For a combination of appropriate parameters, we obtain Fig. 3 where the light grey shaded area indicates realistic values of stress and permeability for buried dolomites. The upper and lower dark grey shaded areas indicate the regions in which no banding will be observed, either because equation 3 remains stable without periodic waves in the solution (stable area) or the distance between the layers is too narrow (critical spacing) to produce macroscopically visible bands as the spacing would be on the order of the grain size ($\sim 100\ \mu\text{m}$).

We can now quantify the relationship between permeability, overpressure and the density of bands. The overpressure in San Vicente is related to a burial depth of about 3 km which is the maximum burial depth of the strata hosting the zebra dolomites¹⁷. The yield stress can be defined as the point at which the material permanently deforms by 0.2%⁴⁵. This state should be reached at relatively low stresses for dolomites and therefore the overpressure ($\sigma - \sigma_y$) can be assumed to show only moderate fluctuation around the maximum pressure. The remaining critical parameter is the permeability, which is related to the porosity of the rock⁴⁶. A variation of this parameter can explain the difference in band spacing and thickness (Fig. 1a). Additionally, the spatial localization of the zebra texture, which is observable in Fig. 1b,d, can be explained by local permeability contrasts.

The development of the compaction bands out of an initially heterogeneous rock is the primary stage of the pattern formation. The compaction bands have a higher permeability compared to the surrounding host rock and fluid flow as well as dissolution/precipitation processes will be focused inside these channels due to elevated fluid pressure. We hypothesise that, due to the development of the compaction instabilities, a local recrystallization takes place. During this process, the pre-existing impurities in the dolomite are washed out and accumulate outside of the channels (Fig. 1b). This is in good agreement with the findings of^{25,27} who interpreted the light

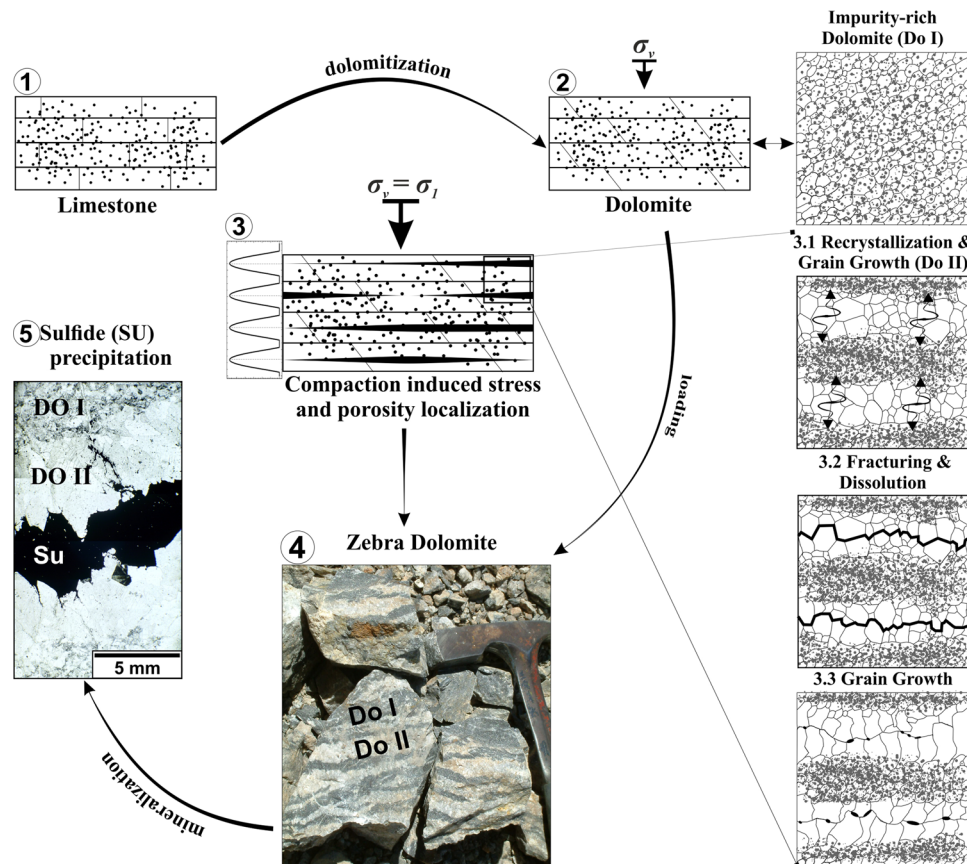


Figure 4. Conceptual model of zebra texture formation in dolomite involving the development of compaction instabilities leading to focused recrystallization and subsequent grain growth affected by second-phase particle densities. An impurity-rich limestone (1) is dolomitized by an infiltrating fluid (2). This fluid-saturated dolomite (*Do I*) undergoes compaction during burial, and instabilities evolve as soon as the critical values of permeability and loading are reached (3). The small plot next to sketch number 3 indicates how the solution of equation 3 is related to the localisation of high-porosity and high-pressure channels. Recrystallization is then focused in equidistant channels (*Do II*) whereas the second-phase is washed out and accumulated between the channels (3.1). The subsequent grain growth is now focused in the areas of low impurity densities. The high pressure then leads to fracturing in the high-pressure channels of the compaction bands as the yield stress is successively lowered during grain coarsening (*Hall-Petch relation*^{50,51}). The highest pressures occur in the centre of the compaction instabilities leading to fracturing and subsequent dissolution along the median line of the coarse grained layers (3.2). The grain growth continues whereas the grains now elongate towards the central line where stress is depleted due to the fracturing (3.3). The resulting texture is periodically layered (4). If a mineralizing fluid percolates into this structure, the sulphide (Su) will precipitate along the vuggy median line (5).

bands as dissolution or recrystallization features that develop during focused fluid flow. However, our model does not require pulsed expulsion of fluids²⁷ or the development of en-echelon fractures^{22,25,27}. The grain growth process will affect the whole rock volume but will be favoured in areas of low impurity densities⁴⁷, and therefore inside the compaction bands. Grain boundary migration in systems that are comprised of a layered distribution of second-phase material can produce structures which are very similar to the zebra dolomites⁴⁸. We argue that a fracture can also develop in the central part of the impurity depleted coarsening layers (Fig. 1c), because the fluid pressure is at its highest in the central part of the compaction band and the breaking strength of the material decreases with increasing grain size⁴⁹. This can quantitatively be described by the *Hall-Petch effect*^{50,51}, that gives a relationship between yield stress and crystal size. A developing crack is accompanied by a stress drop in the solid around the fracture. As grain growth is sensitive to stress, the crystals will tend to elongate towards this crack (Fig. 1e)⁵². Even without material failure, dissolution will occur in the central part of the coarse layer in response to the elevated fluid pressure. Such dissolution features were reported for several zebra dolomite occurrences^{16,25,26,32} and crack-like structures filled with a late carbonate phase are shown in Fig. 1c.

Towards an integrative model of zebra dolomite formation. We presented a generic model of zebra dolomite formation (Fig. 4) based on the compaction band theory^{11,40} coupled with a reaction-diffusion model (see also Alevizos *et al.*⁴³ for more details). In detail, our model is based on local dissolution-precipitation dynamics and, in contrast to other theories^{19,20,28}, does not require displacive vein growth for the band's equidistant

spacing to occur. Our model also does not rely on initial sedimentary partings²¹ or the development of fracture networks¹⁵ (see supplementary material for further discussion).

We were able to show that the spacing of bands is a function of permeability and/or stress variations. Our approach is capable of integrating the findings of other works^{16,18–20,22,25–28,46} and it successfully explains all the specific features of the pattern. The layered distribution of impurities is caused by the focused recrystallization inside the compaction bands (Fig. 4.3) and the grain size variation is a direct result of the recrystallization⁴⁸. The elongated shape of the crystals of the light layers is caused by the dissolution and/or fracturing along the central part of the layer (Fig. 4.3.2) as a function of high fluid pressures and large grain sizes. A vuggy porosity along the central line will remain and a late carbonate phase will precipitate in the median line (Fig. 4.3.3). The texture is important for ore mineralization. If a mineralizing fluid percolates into the structure, the sulphides will start precipitating along the median line (Fig. 4.5), which is often observed in the samples.

In line with Turing² we propose a general process of pattern formation based on a reaction-diffusion equation but extended by hydromechanics. The basis of our model is the *Cahn-Hilliard* equation, where the process modelled is phase separation during which domains develop that contain a large amount of one of the two phases, a process that is often accompanied by pattern formation⁵³. In our scenario, these accumulated phases are the impurities in the dark dolomite layers. In contrast to previously published theories on zebra dolomite formation we put forward a mathematical description of the reactive solid-fluid system coupled with hydromechanics. The predictions of our model can be scaled with field observation and we propose that it can represent a new tool for field-geologists to estimate rheological parameters such as permeability and stress. For now being solely a mathematical description, we state that our approach to pattern formation in dolomites represents one of nature's general processes of producing periodic wave-like patterns in natural systems. Furthermore, the inversion routine applied in this communication demonstrates a relationship between the spacing of geological structures such as bands or layers and the fluid pressure and permeability during pattern formation. Having an access to these parameters is of high interest for scientific research as well as for mineral- or hydrocarbon exploration and extraction. In addition to that, the mathematical model predicts that the zebra layers form perpendicular to the main stress direction. It is therefore possible to determine the orientation of the stress-ellipsoid during the pattern formation as well. Thus, the model presented in this study represents the first step towards the development of a new tool for geologists that will help to assess paleo-fluid pressure, paleo-stress and paleo-permeability of geological formations hosting banded or layered structures.

Future exploration of mineral and energy resources will target deposits at greater depth. With increasing depth feedback mechanisms between mechanical compaction and chemical reaction rates will become more important. A complete understanding of the exact mechanisms that are active in such deeper environments will become crucial for successful prediction of deposit location and their exploration. In addition, the extraction of resources from deeper hosts may trigger feedback mechanisms that to date are not fully understood. Striking examples of such feedback mechanism are the production induced compaction in the Ekofisk oil field⁵⁴ and the success of gas extraction in the Cooper Basin, Australia⁵⁵.

References

- Meinhardt, H. Models of biological pattern formation. *Academic Press* (1982).
- Turing, A. M. The Chemical Basis of Morphogenesis. *Philos T Roy Soc B* **237**, 37–72, <https://doi.org/10.1098/rstb.1952.0012> (1952).
- L'Heureux, I. Self-organized rhythmic patterns in geochemical systems. *Philos T R Soc A* **371**, <https://doi.org/10.1098/rsta.2012.0356> (2013).
- Sun, S. & Li, Y.-L. Geneses and evolutions of iron-bearing minerals in banded iron formations of >3760 to ca. 2200 million-year-old: Constraints from electron microscopic, X-ray diffraction and Mössbauer spectroscopic investigations. *Precambrian Res* **289**, 1–17, <https://doi.org/10.1016/j.precamres.2016.11.010> (2017).
- Fu, L., Milliken, K. L. & Sharp, J. M. Porosity and Permeability Variations in Fractured and Liesegang-Banded Breathitt Sandstones (Middle Pennsylvanian), Eastern Kentucky - Diagenetic Controls and Implications for Modeling Dual-Porosity Systems. *J Hydrol* **154**, 351–381, [https://doi.org/10.1016/0022-1694\(94\)90225-9](https://doi.org/10.1016/0022-1694(94)90225-9) (1994).
- Ohkawa, M., Yamashita, Y., Inoue, M., Kitagawa, R. & Takeno, S. Hematite in pyrophyllite ore deposits, Shobara district, southwestern Japan. *Miner Petrol* **70**, 15–23, <https://doi.org/10.1007/s007100070010> (2000).
- Montési, L. G. J. A constitutive model for layer development in shear zones near the brittle-ductile transition. *Geophysical Research Letters* **34**, <https://doi.org/10.1029/2007GL029250> (2007).
- Ortoleva, P., Chadam, J., Merino, E. & Sen, A. Geochemical Self-Organization .2. The Reactive-Infiltration Instability. *Am J Sci* **287**, 1008–1040 (1987).
- Ortoleva, P., Merino, E., Moore, C. & Chadam, J. Geochemical Self-Organization .1. Reaction-Transport Feedbacks and Modeling Approach. *Am J Sci* **287**, 979–1007 (1987).
- Wang, Y. F. & Budd, D. A. Stress-induced chemical waves in sediment burial diagenesis. *Nat Commun* **3**, <https://doi.org/10.1038/ncomms1684> (2012).
- Veveakis, E. & Regenauer-Lieb, K. Cnoidal waves in solids. *J Mech Phys Solids* **78**, 231–248, <https://doi.org/10.1016/j.jmps.2015.02.010> (2015).
- Loughnan, F. C. & Roberts, F. I. Composition and Origin of the Zebra Rock from the East Kimberley Region of Western-Australia. *Aust J Earth Sci* **37**, 201–205, <https://doi.org/10.1080/08120099008727920> (1990).
- Krug, H. J., Brandtstadter, H. & Jacob, K. H. Morphological instabilities in pattern formation by precipitation and crystallization processes. *Geol Rundsch* **85**, 19–28, <https://doi.org/10.1007/s005310050047> (1996).
- Palinkas, S. S., Spangenberg, J. E. & Palinkas, L. A. Organic and inorganic geochemistry of Ljubija siderite deposits, NW Bosnia and Herzegovina. *Miner Deposita* **44**, 893–913, <https://doi.org/10.1007/s00126-009-0249-z> (2009).
- Wallace, M. W., Both, R. A., Ruano, S. M. & Hachali, P. F. Zebra Textures from Carbonate-Hosted Sulfide Deposits - Sheet Cavity Networks Produced by Fracture and Solution Enlargement. *Econ Geol Bull Soc* **89**, 1183–1191 (1994).
- Fontboté, L. in *Current research in geology applied to ore deposits. Proceedings of the Second Biennial SGA Meeting* (eds J. Torres-Ruiz P.Fenoll Hach-Ali & F. Gervilla) 11–14 (1993).
- Fontboté, L. & Gorzawski, H. Genesis of the Mississippi Valley-Type Zn-Pb Deposit of San Vicente, Central Peru - Geologic and Isotopic (Sr, O, C, S, Pb) Evidence. *Econ Geol Bull Soc* **85**, 1402–1437 (1990).
- Lopez-Horgue, M. A. *et al.* Structurally controlled hydrothermal dolomites in Albian carbonates of the Ason valley, Basque Cantabrian Basin, Northern Spain. *Mar Petrol Geol* **27**, 1069–1092, <https://doi.org/10.1016/j.marpetgeo.2009.10.015> (2010).

19. Merino, E. & Canals, A. Self-Accelerating Dolomite-for-Calcite Replacement: Self-Organized Dynamics of Burial Dolomitization and Associated Mineralization. *Am J Sci* **311**, 573–607, <https://doi.org/10.2475/07.2011.01> (2011).
20. Merino, E., Canals, A. & Fletcher, R. C. Genesis of self-organized zebra textures in burial dolomites: Displacive veins, induced stress, and dolomitization. *Geol Acta* **4**, 383–393 (2006).
21. Morrow, D. W. Zebra and boxwork fabrics in hydrothermal dolomites of northern Canada: Indicators for dilational fracturing, dissolution or *in situ* replacement? *Sedimentology* **61**, 915–951, <https://doi.org/10.1111/sed.12094> (2014).
22. Badoux, V., Moritz, R. & Fontboté, L. The Mississippi Valley-type Zn-Pb deposit of San Vicente, Central Peru: an Andean syntectonic deposit. *Mineral deposits at the beginning of the 21st Century. Proceed Joint 6th Biennial SGA-SEG Mtg, Krakow, Poland*, 191–195 (2001).
23. Diehl, S. F. *et al.* Hydrothermal Zebra Dolomite in the Great Basin, Nevada-Attributes and Relation to Paleozoic Stratigraphy, Tectonics, and Ore Deposits. *Geosphere* **6**, 663–690, <https://doi.org/10.1130/Ges00530.1> (2010).
24. Leach, D. L. & Viets, J. G. Comparison of the Cracow-Silesian Mississippi Valley-type district, southern Poland, with Mississippi Valley-type districts in North America. *Open-File Report OF/92* **704**, 72 (1992).
25. Nielsen, P., Swennen, R., Muchez, P. H. & Keppens, E. Origin of Dinantian zebra dolomites south of the Brabant-Wales Massif, Belgium. *Sedimentology* **45**, 727–743 (1998).
26. Swennen, R., Vandeginste, V. & Ellam, R. Genesis of zebra dolomites (Cathedral Formation: Canadian Cordillera Fold and Thrust Belt, British Columbia). *J Geochem Explor* **78–9**, 571–577, [https://doi.org/10.1016/S0375-6742\(03\)00065-7](https://doi.org/10.1016/S0375-6742(03)00065-7) (2003).
27. Vandeginste, V. *et al.* Zebra dolomitization as a result of focused fluid flow in the Rocky Mountains Fold and Thrust Belt, Canada. *Sedimentology* **52**, 1067–1095, <https://doi.org/10.1111/j.1365-3091.2005.00724.x> (2005).
28. Merino, E. Self-accelerating dolomite-for-calcite replacement and displacive zebra veins: Dynamics of burial dolomitization. *Geochim Cosmochim Acta* **70**, A417–A417, <https://doi.org/10.1016/j.gca.2006.06.839> (2006).
29. Anderson, G. M. & Macqueen, R. W. Ore Deposit Models -6. Mississippi Valley-Type Lead-Zinc Deposits. *Geosci Can* **9**, 108–117 (1982).
30. Bradley, D. C. & Leach, D. L. Tectonic controls of Mississippi Valley-type lead-zinc mineralization in orogenic forelands. *Miner Deposita* **38**, 652–667, <https://doi.org/10.1007/s00126-003-0355-2> (2003).
31. Leach, D. L., Taylor, R. D., Diehl, S. F. & Saltus, R. W. A deposit model for Mississippi Valley-Type lead-zinc ores, chap. A of Mineral deposit models for resource assessment: U.S. Geological Survey Scientific Investigations Report 2010–5070–A, 52 (2010).
32. Nader, F. H. *et al.* The Ranero Hydrothermal Dolomites (Albian, Karrantza Valley, Northwest Spain): Implications on Conceptual Dolomite Models. *Oil Gas Sci Technol* **67**, 9–29, <https://doi.org/10.2516/ogst/2011165> (2012).
33. Rosas, S., Fontboté, L. & Tankard, A. Tectonic evolution and paleogeography of the Mesozoic Pucara Basin, central Peru. *J S Am Earth Sci* **24**, 1–24, <https://doi.org/10.1016/j.jsames.2007.03.002> (2007).
34. Spangenberg, J., Fontboté, L., Sharp, Z. D. & Hunziker, J. Carbon and oxygen isotope study of hydrothermal carbonates in the zinc-lead deposits of the San Vicente district, central Peru: a quantitative modeling on mixing processes and CO₂ degassing. *Chem Geol* **133**, 289–315, [https://doi.org/10.1016/S0009-2541\(96\)00106-4](https://doi.org/10.1016/S0009-2541(96)00106-4) (1996).
35. Putnis, C. V., Ruiz-Agudo, E. & Hövelmann, J. Coupled fluctuations in element release during dolomite dissolution. *Mineralogical Magazine* **78**, 1355–1362, <https://doi.org/10.1180/minmag.2014.078.6.01> (2014).
36. Ho, C.-D., Yeh, H.-M. & Yeh, T.-L. The optimal variation of zone lengths in multipass zone refining processes. *Separation and Purification Technology* **15**, 69–78, [https://doi.org/10.1016/S1383-5866\(98\)00084-7](https://doi.org/10.1016/S1383-5866(98)00084-7) (1999).
37. Jessell, M. W., Kostenko, O. & Jamtveit, B. The preservation potential of microstructures during static grain growth. *J Metamorph Geol* **21**, 481–491, <https://doi.org/10.1046/j.1525-1314.2003.00455.x> (2003).
38. Koehn, D., Malthe-Sørensen, A. & Passchier, C. W. The structure of reactive grain-boundaries under stress containing confined fluids. *Chem Geol* **230**, 207–219, <https://doi.org/10.1016/j.chemgeo.2006.02.026> (2006).
39. McKenzie, D. The Generation and Compaction of Partially Molten Rock. *J Petrol* **25**, 713–765 (1984).
40. Veveakis, E., Regenauer-Lieb, K. & Weinberg, R. F. Ductile compaction of partially molten rocks: the effect of non-linear viscous rheology on instability and segregation. *Geophys J Int* **200**, 519–523, <https://doi.org/10.1093/gji/ggu412> (2015).
41. Weinberg, R. F., Veveakis, E. & Regenauer-Lieb, K. Compaction-driven melt segregation in migmatites. *Geology* **43**, 471–474, <https://doi.org/10.1130/G36562.1> (2015).
42. Abramowitz, M. & Stegun, I. A. *Handbook of mathematical functions: with formulas, graphs, and mathematical tables*. Vol. 55 (Courier Corporation, 1964).
43. Alevizos, S. *et al.* A Framework for Fracture Network Formation in Overpressurised Impermeable Shale: Deformability Versus Diagenesis. *Rock Mechanics and Rock Engineering*, 1–15, <https://doi.org/10.1007/s00603-016-0996-y> (2016).
44. Lvov, B. V. *Thermal decomposition of solids and melts: new thermochemical approach to the mechanism, kinetics and methodology*. Vol. 7 209 (Springer Science & Business Media, 2007).
45. Mogi, K. Fracture and flow of rocks. *Tectonophysics* **13**, 541–568, [https://doi.org/10.1016/0040-1951\(72\)90037-6](https://doi.org/10.1016/0040-1951(72)90037-6) (1972).
46. Warren, J. Dolomite: occurrence, evolution and economically important associations. *Earth-Science Reviews* **52**, 1–81, [https://doi.org/10.1016/S0012-8252\(00\)00022-2](https://doi.org/10.1016/S0012-8252(00)00022-2) (2000).
47. Evans, B., Renner, J. & Hirth, G. A few remarks on the kinetics of static grain growth in rocks. *Int J Earth Sci* **90**, 88–103 (2001).
48. Kelka, U., Koehn, D. & Beaudoin, N. Zebra pattern in rocks as a function of grain growth affected by second-phase particles. *Frontiers in Physics* **3**, <https://doi.org/10.3389/fphy.2015.00074> (2015).
49. Renner, J. & Evans, B. Do calcite rocks obey the power-law creep equation? *Deformation Mechanisms, Rheology and Tectonics: Current Status and Future Perspectives* **200**, 293–307, <https://doi.org/10.1144/Gsl.Sp.2001.200.01.17> (2002).
50. Hall, E. O. The Deformation and Ageing of Mild Steel .3. Discussion of Results. *P Phys Soc Lond B* **64**, 747–753, <https://doi.org/10.1088/0370-1301/64/9/303> (1951).
51. Petch, N. J. The Cleavage Strength of Polycrystals. *J Iron Steel I* **174**, 25–28 (1953).
52. Bons, P. D., Elburg, M. A. & Gomez-Rivas, E. A review of the formation of tectonic veins and their microstructures. *J Struct Geol* **43**, 33–62, <https://doi.org/10.1016/j.jsg.2012.07.005> (2012).
53. Novick-Cohen, A. in *Handbook of Differential Equations: Evolutionary Equations* Vol. Volume 4 (eds M. Dafermos Constantine & Pokorný Milan) 201–228 (North-Holland, 2008).
54. Keszthelyi, D., Dysthe, D. K. & Jamtveit, B. Compaction of North-Sea Chalk by Pore-Failure and Pressure Solution in a Producing Reservoir. *Frontiers in Physics* **4**, <https://doi.org/10.3389/fphy.2016.00004> (2016).
55. Veveakis, M., Poulet, T. & Regenauer-Lieb, K. In *International Conference and Exhibition, Melbourne, Australia 13-16 September 2015*. 211–211 (Society of Exploration Geophysicists and American Association of Petroleum Geologists).
56. Paradis, S., Hannigan, P. & Dewing, K. Mississippi Valley-type lead-zinc deposits. *Mineral deposits of Canada: A synthesis of major deposit-types, district metallogeny, the evolution of geological provinces, and exploration methods: Geological Association of Canada, Mineral Deposits Division, Special Publication* **5**, 185–203 (2007).
57. Kestin, J., Khalifa, H. E. & Correia, R. J. Tables of the Dynamic and Kinematic Viscosity of Aqueous NaCl Solutions in the Temperature-Range 20–150°C and the Pressure Range 0.1–35 Mpa. *J Phys Chem Ref Data* **10**, 71–87 (1981).
58. Gautelier, M., Oelkers, E. H. & Schott, J. An experimental study of dolomite dissolution rates as a function of pH from –0.5 to 5 and temperature from 25 to 80°C. *Chem Geol* **157**, 13–26, [https://doi.org/10.1016/S0009-2541\(98\)00193-4](https://doi.org/10.1016/S0009-2541(98)00193-4) (1999).
59. Arvidson, R. S. & Mackenzie, F. T. The dolomite problem: Control of precipitation kinetics by temperature and saturation state. *Am J Sci* **299**, 257–288, <https://doi.org/10.2475/ajs.299.4.257> (1999).

Acknowledgements

We would like to thank Dr. Thomas Poulet and Prof. Klaus Regenauer-Lieb for fruitful discussions during the development of the analytical model. We would further like to thank Dr. Julien Plancq, Dr. Susan Fitzer and Prof. Piotr Szymczak for their helpful comments on the manuscript. The comments of the three reviewers helped a lot to improve this paper in terms of accuracy and illustrative examples. This research has received funding from the European Union's Seventh Framework Programme under grant agreement no. 316889.

Author Contributions

Author names appear in the order of their contribution to the respective subject. Development of the analytical model: Manolis Veveakis, Ulrich Kelka. Data collection: Daniel Koehn, Ulrich Kelka. Data analysis and interpretation: Ulrich Kelka, Daniel Koehn, Nicolas Beaudoin. Drafting the article: Ulrich Kelka, Manolis Veveakis, Daniel Koehn. Critical revision of the article: Daniel Koehn, Nicolas Beaudoin.

Additional Information

Supplementary information accompanies this paper at <https://doi.org/10.1038/s41598-017-14541-3>.

Competing Interests: The authors declare that they have no competing interests.

Publisher's note: Springer Nature remains neutral with regard to jurisdictional claims in published maps and institutional affiliations.



Open Access This article is licensed under a Creative Commons Attribution 4.0 International License, which permits use, sharing, adaptation, distribution and reproduction in any medium or format, as long as you give appropriate credit to the original author(s) and the source, provide a link to the Creative Commons license, and indicate if changes were made. The images or other third party material in this article are included in the article's Creative Commons license, unless indicated otherwise in a credit line to the material. If material is not included in the article's Creative Commons license and your intended use is not permitted by statutory regulation or exceeds the permitted use, you will need to obtain permission directly from the copyright holder. To view a copy of this license, visit <http://creativecommons.org/licenses/by/4.0/>.

© The Author(s) 2017